EXTREME-ULTRAVIOLET OBSERVATIONS OF GLOBAL CORONAL WAVE ROTATION

G. D. R. Attrill[1], D. M. Long[2], L. M. Green[2], L. K. Harra[2], and L. van Driel-Gesztelyi[2,3,4]

[1] Defence Science and Technology Laboratory, Dstl Porton Down, Salisbury, Wiltshire SP4 0JQ, UK; gdrattrill@dstl.gov.uk
[2] University College London, Mullard Space Science Laboratory, Holmbury St. Mary, Dorking, Surrey RH5 6NT, UK
[3] Observatoire de Paris, LESIA, CNRS, F-92195 Meudon, France
[4] Konkoly Observatory, Hungarian Academy of Sciences, Budapest, Hungary

ABSTRACT

We present evidence of global coronal wave rotation in EUV data from *SOHO*/EIT, *STEREO*/EUVI, and *SDO*/AIA. The sense of rotation is found to be consistent with the helicity of the source region (clockwise for positive helicity, anticlockwise for negative helicity), with the source regions hosting sigmoidal structures. We also study two coronal wave events observed by *SDO*/AIA where no clear rotation (or sigmoid) is observed. The selected events show supporting evidence that they all originate with flux rope eruptions. We make comparisons across this set of observations (both with and without clear sigmoidal structures). On examining the magnetic configuration of the source regions, we find that the nonrotation events possess a quadrupolar magnetic configuration. The coronal waves that do show a rotation originate from bipolar source regions.

Key words: Sun: corona – Sun: coronal mass ejections (CMEs) – Sun: magnetic fields

1. INTRODUCTION

Almost a decade after its initial discovery, the much-studied 1997 May 12 coronal wave was shown to have a systematic angular displacement in time counterclockwise by Podladchikova & Berghmans (2005). This observation demonstrated that this coronal wave not only propagates radially but also rotates as it expands. The 1997 May 12 coronal mass ejection (CME) source region was located in the northern hemisphere in AR 8038, which exhibited a pre-eruption reverse "S" sigmoidal structure (Rust & Kumar 1996), often cited as an indicator of left-handed twist/negative helicity (Pevtsov et al. 1997; Leamon et al. 2002).

Attrill et al. (2007) independently confirmed the finding of Podladchikova & Berghmans (2005), and additionally studied the 1997 April 7 coronal wave event. The CME associated with this event originated from AR 8027, located in the southern hemisphere, where a pre-eruption forward "S" (positive helicity) sigmoidal structure is visible in EUV imager data. This coronal wave was found to display a clockwise rotation as it expanded.

The nature of coronal waves is much debated. Gallagher & Long (2011) give a recent review of the various theories (see also Liu & Ofman 2014; Patsourakos & Vourlidas 2012; Zhukov 2011; Wills-Davey & Attrill 2009). When "EIT waves" were first observed (Thompson et al. 1998), it was suggested that they could be the flare-induced coronal counterpart of the hydrodynamic chromospheric Moreton fast shock wave (Moreton 1960; Moreton & Ramsey 1960), the existence of which had been predicted by Uchida (1968). More recent statistical studies (Biesecker et al. 2002; Cliver et al. 2005) have shown "EIT waves" to be more closely associated with CMEs than with flares. The apparent relationship between the sense of coronal wave rotation and the helicity of the CME source region (Attrill et al. 2007) supported the view that coronal waves were CME-driven, rather than the historically popular interpretation as a flare-initiated blast wave. The current consensus is that at least part of the bright front constituting the "EIT wave" is due to a wavefront driven by rapid expansion of the CME in the low corona. Later this becomes freely propagating (e.g., Patsourakos et al. 2010; Downs et al. 2012).

In this paper, we examine six global coronal wave events to see if the relationship Attrill et al. (2007) found between the sense of coronal wave rotation and source regions helicity for the 1997 April 7 and May 12 events holds for a larger sample. As in that paper, we select CME source regions where there is supporting evidence for the existence of pre-eruption flux ropes.

2. DATA

This analysis utilizes EUV data from three current missions: the *Solar and Heliospheric Observatory* (*SOHO*; Domingo et al. 1995); the *Solar Terrestrial Relations Observatory* (*STEREO*; Kaiser et al. 2008; Driesman et al. 2008), and the *Solar Dynamics Observatory* (*SDO*; Pesnell et al. 2012).

2.1. SOHO/EIT Data

The Extreme Ultraviolet (EUV) Imaging Telescope (EIT; Delaboudinière et al. 1995) is a normal incidence telescope, imaging at 171 Å, 195 Å, 284 Å, and 304 Å that is designed to study the dynamics and evolution of coronal structures over a wide range of timescales, sizes, and temperatures. EIT returns EUV images of the corona and transition region on the solar disk and up to 1.5 $R_\odot$ above the solar limb with a 45′ × 45′ square field of view. EIT has a maximum spatial resolution, imaging 1024 × 1024 pixels of 2″.63 each, though on-chip binning, which reduces the resolution by half to improve the cadence (imaging 512 × 512 pixels of 5″.26 each), is also commonly used (Moses et al. 1997). The cadence for EIT images can vary, but for the data used in this paper there are typically 12 minutes between frames.

2.2. STEREO/EUVI Data

The identical EUV Imaging (EUVI; Wülser et al. 2004) normal incidence telescopes on the two *STEREO* spacecraft are designed to study the structure and evolution of the solar corona in three dimensions, and specifically to focus on the initiation and early evolution of CMEs. The EUVI's 2048 × 2048 pixel CCD detectors (with 1″.59 pixel size) have a field of view out to 1.7 $R_\odot$, and observe in four spectral channels (deliberately chosen to match those of *SOHO*/EIT) spanning a temperature
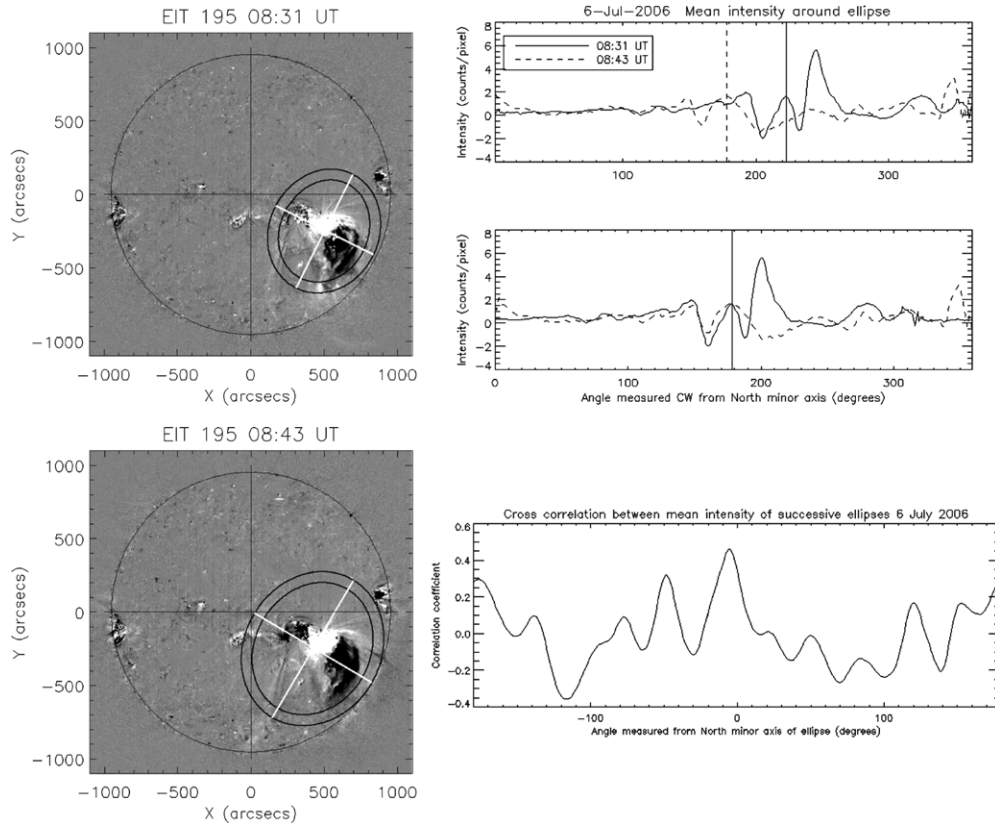
Figure 1. Left panels show the 2006 July 6 coronal wave expansion. The top right panel shows the mean intensity measured around the ellipse at 08:31 and 08:43 UT. The center right panel shows a phase shift of −41° applied to the earlier intensity plot. The bottom right panel shows the automatically calculated cross-correlation between the two mean intensity traces.

range of 1×10^5 K to 2×10^7 K. In addition to its view from two vantage points, the EUVI therefore provides a substantial improvement in image resolution and image cadence over its predecessor *SOHO*/EIT (EUVI can be run at an ∼2 minute cadence).

2.3. SDO/AIA Data

The Atmospheric Imaging Assembly (AIA; Lemen et al. 2012) comprises four normal incidence telescopes that take full-disk images of the solar corona, up to at least 0.3 $R_\odot$ above the solar limb, producing 4096 × 4096 pixel images at 1″ resolution. AIA is able to observe across a broad temperature range of approximately 20,000 K to >20 × 10^6 K by imaging in seven EUV passbands (94 Å, 131 Å, 171 Å, 193 Å, 211 Å, 304 Å, 335 Å) and three UV passbands (1600 Å, 1700 Å and 4500 Å). The AIA image cadence returns full-disk images in each of these 10 wavelengths every 12 s.

3. METHODOLOGY

We use the method described in Attrill et al. (2007) to analyze the coronal wave events. The coronal wave of each event is captured in two successive EUV base difference images. We use running difference images to identify short-term transient features of interest, but base difference images (corrected for solar rotation) to analyze intensity. Running difference images can show false brightenings and dimmings (e.g., Chertok & Grechnev 2005), and can make it difficult to differentiate real features from optical illusions (e.g., Attrill 2010). We analyze the intensity of the coronal wavefront as a function of azimuthal angle around the wavefront. We assume an isotropic, circular

expansion around an epi-center and account for line-of-sight (LOS) projection effects (e.g., Deforest 2004). As a result, a circular coronal wave is observed as an ellipse in projection. The projection of the coronal wave changes as it expands across the solar disk; thus, using the projected azimuthal angle can induce a fake rotation. To avoid this, we plot the intensity as a function of the deprojected azimuthal angle (in the plane perpendicular to the local vertical at the epicenter of the wave, i.e., the azimuthal angle around the real circle). The axes of the ellipse are used as a reference for the azimuthal angle. Full details of the compensation made for projection effects are described in Attrill (2008).

The ellipse characteristics are defined by the initial location of the eruption and by the angular radius, δ, of the coronal wave (the half-cone angle subtended at the center of the solar sphere). We sum the intensity, I, of the ring defined by the black ellipses (e.g., as shown in Figure 1). By changing δ and systematically shifting the center of the ellipse about the initial epi-center (taken as the location of the associated flare) we objectively find the best values for the center and δ of the ellipse, which capture most of the coronal wave intensity. Where possible, this process is automated. For some of the events (details in the following sections), the location of a key feature (e.g., a neighboring coronal hole or active region) skews this automated process. In these cases, the δ of the ellipse (still constrained as described above), is varied by hand to ensure the correct feature (i.e., the coronal wave bright front) is being sampled.

The data are averaged in both the radial direction, from the inner to the outer ellipse and in the azimuthal direction (around the ellipse), using boxcar smoothing with a smoothing kernel of 11°. The top right panels of Figures 1–4 show the mean intensity
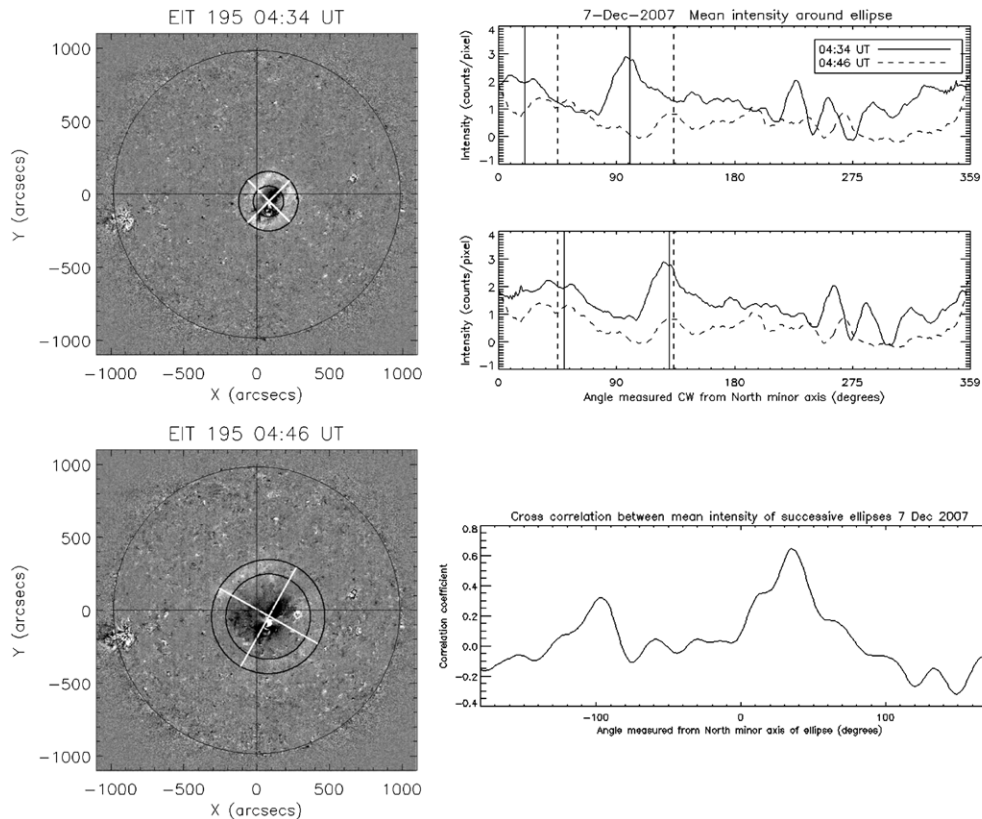
Figure 2. Left panels show the 2007 December 7 coronal wave expansion. The top right panel shows the mean intensity measured around the ellipse at 04:34 and 04:36 UT. The center right panel shows a phase shift of +29° applied to the earlier intensity plot. The bottom right panel shows the automatically calculated cross-correlation between the two mean intensity traces.

of the ring plotted as a function of the deprojected azimuthal angle for two EUV images in which the coronal wave is visible. The vertical lines mark the weighted mean for each peak. The center right panels of Figures 1–4 show the weighted mean of the intensity of the earlier coronal wave front peak(s) phase-shifted to match those of the later coronal wave front peak(s). The bottom right panels of Figures 1–4 show the cross-correlation values between the two mean intensity data sets, computed using the IDL routine *c_correlate*. This function computes the cross-correlation of two sample populations as a function of specified values of the lag between them. For this analysis, the lag is set from −180° to +180°.

Ideally, EUV imaging data showing "textbook" events similar to the 1997 May 12 coronal wave were selected for this analysis. Isolated source regions surrounded by quiet Sun, expanding over the solar disk, were the most desirable candidates. Table 1 details other events that were considered, but on closer inspection ruled out, for this analysis. Event-specific details for the six coronal waves analyzed are described in the following sub-sections.

4. CORONAL WAVE EVENTS

Table 2 summarizes the key points for each event described in this section. Details include the helicity of the CME source region, and the direction of the rotation (as measured "by eye" and also that computed automatically by employing cross-correlation).

4.1. 2006 July 6

The 2006 July 6 coronal wave event was associated with a halo CME, which originated from NOAA AR 10898. An M2.5

class flare was also observed, starting at 08:13 UT. The classical "double dimmings" (also known as "transient coronal holes"; Rust 1983) that develop during this event were studied by Jiang et al. (2007), and the recovery phase has been examined by McIntosh et al. (2007) and Attrill et al. (2008).

Török et al. (2013) followed the evolution of the NOAA AR 10898 in the days preceding this eruption, in particular noting a counter-clockwise rotation of the leading sunspot. Prior to the eruption, a reverse "S" sigmoidal structure was visible at the location of the CME source region (see the top left panel of Figure 5). The observations and modeling of Török et al. (2013) both support the presence of a flux rope with negative helicity.

The coronal wave for the 2006 July 6 event was captured in two successive EIT 195 Å base difference images (Figure 1), at 08:31 UT and 08:43 UT. The base image used was at 08:07 UT, just prior to the start of the eruption. The tilt (from N–S solar axis to N–S minor ellipse axis) is measured as −63°, at 08:31 UT, and −59°, at 08:43 UT. This change in the tilt (+4°) of the minor ellipse axis between frames is taken into account in the analysis of this event (as are the corresponding tilt changes for the remaining events detailed in Table 3).

A concentrated bright point is observed in the base difference image at 08:31 UT, approximately due south of the source active region. However, this concentrated feature did not appear in the second base difference image at 08:43 UT; thus, it is ignored for this comparative analysis, since it is not a common feature. Instead, focusing on other well-defined peaks, a "by-eye" phase shift of ∼−41° (41° anticlockwise) is measured (top and center right panels of Figure 1).

The bottom right panel of Figure 1 shows the automatically computed cross-correlation. Similar to the manual analysis, the
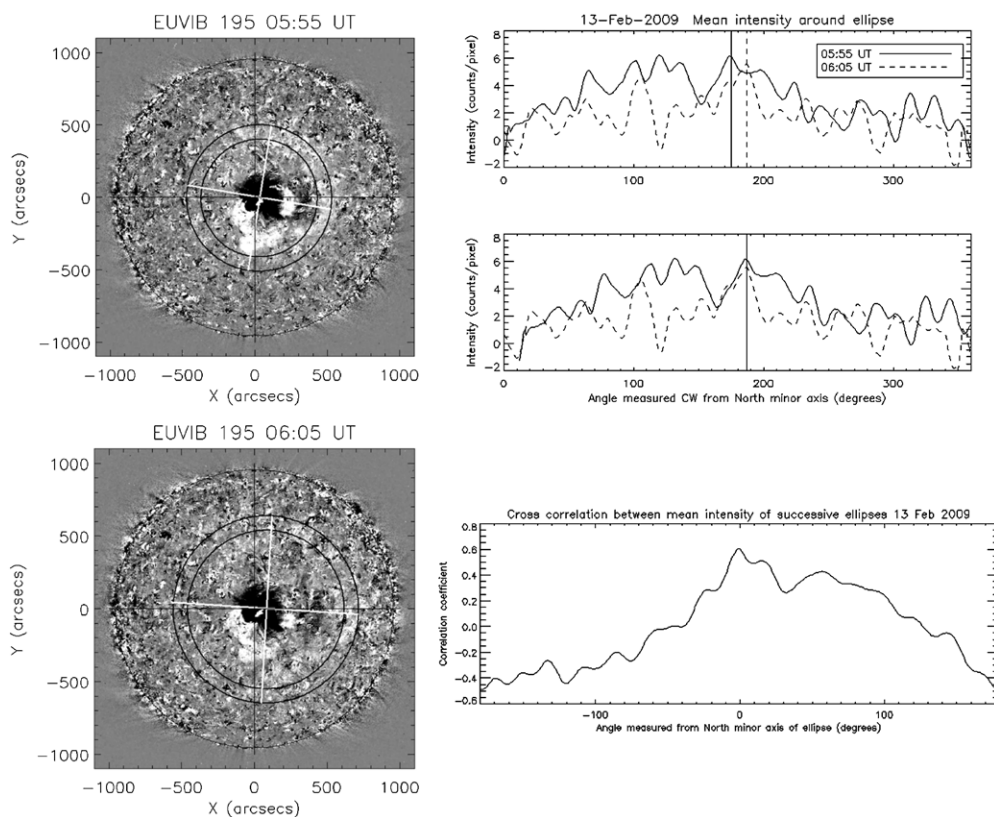
Figure 3. Left panels show the 2009 February 13 coronal wave expansion. The top right panel shows the mean intensity measured around the ellipse at 05:55 and 06:05 UT. The center right panel shows a phase-shift of +12° applied to the earlier intensity plot. The bottom right panel shows the automatically calculated cross-correlation between the two mean intensity traces.
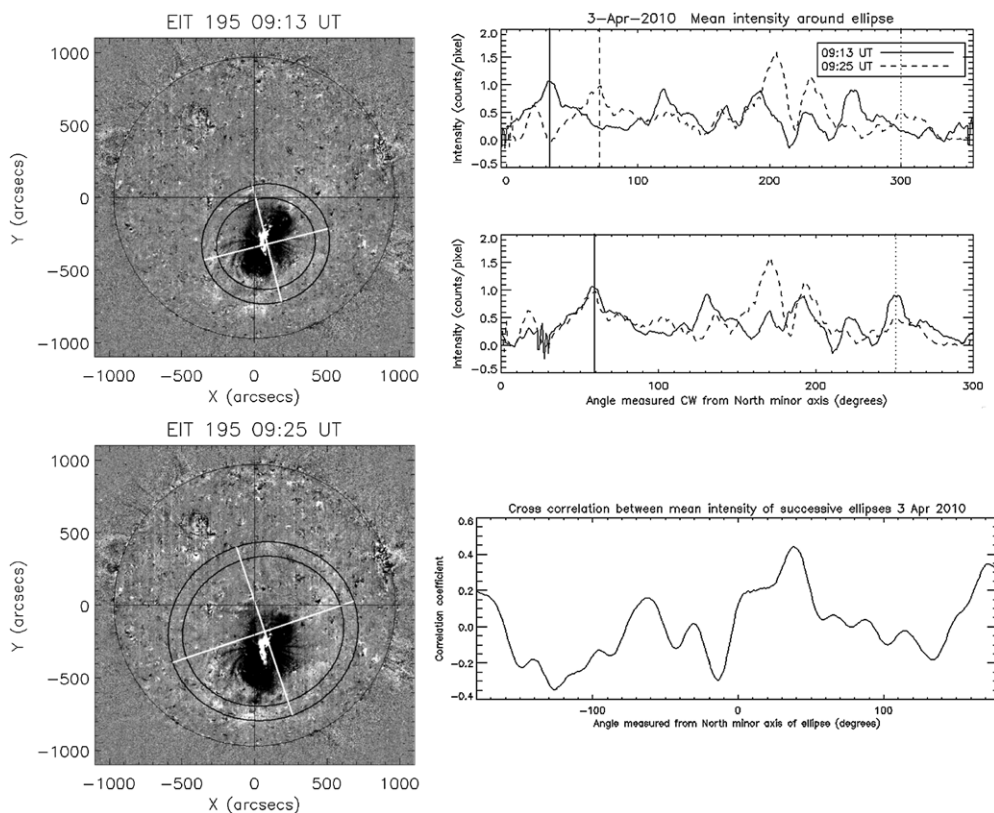

Figure 4. Left panels show the 2010 April 3 coronal wave expansion. The top right panel shows the mean intensity measured around the ellipse at 09:13 and 09:25 UT. The center right panel shows a phase shift of +35° applied to the earlier intensity plot. The bottom right panel shows the automatically calculated cross-correlation between the two mean intensity traces.

Table 1
Coronal Wave Events Examined, But Not Selected, for Analysis

Event	Data Source	Location	Clear Coronal Wave?	Notes
1998 Apr 27	*SOHO*/EIT	SE quadrant	Yes	Two-part eruption, first north, then to the south. Too close to the limb for robust analysis.
2000 Sep 16	*SOHO*/EIT	Center disk	Yes	Two coronal holes both north and south of the source region, plus structured surrounding corona.
2004 Nov 6 and 7	*SOHO*/EIT	Center disk	Yes	Harra et al. (2007) found that eruptions from the same active region, on successive days, produced oppositely directed magnetic clouds. *SOHO*/EIT data indicates the presence of coronal waves accompanying both CMEs, however these events were not selected for this study due to the existence of a very large transequatorial coronal hole, essentially linking the polar regions and wrapping around the north, east and south of the source active region.
2007 May 19	*STEREO*/EUVI(B)	Center disk	Yes	Attrill (2010) found this coronal wave event to comprise two closely-initiated CMEs and two coronal wave events, rather than a single semi-isotropic expansion.
2011 Feb 14	*SDO*/AIA	Center disk	Yes	Asymmetric coronal wave expansion, to the north of the source region only.

Table 2
Summary of Coronal Wave Events: Rotation Properties

Event	Helicity of CME Source Region	Measured "by eye" Rotation	Computed Cross-correlation Rotation
2006 Jul 6	Negative	41° anticlockwise	48° anticlockwise
2007 Dec 7	Positive	29° clockwise	35° clockwise
2009 Feb 13	Positive	12° clockwise	15° clockwise
2010 Apr 3	Positive	35° clockwise	38° clockwise
2011 Feb 13	Positive	None measurable	15° anticlockwise
2011 Feb 15	Positive	None measurable	2° clockwise

Table 3
Details of the Measured Tilt from N–S Solar Axis to N–S Minor Ellipse Axis for Each Coronal Wave Event

Event	1st Frame Time and Tilt	2nd Frame Time and Tilt	3rd Frame Time and Tilt
2006 Jul 6	08:31 UT; −63°	08:43 UT; −59°	· · ·
2007 Dec 7	04:34 UT; −45°	04:46 UT; −59°	· · ·
2009 Feb 13	05:55 UT; −81°	06:05 UT; −86°	· · ·
2010 Apr 3	09:13 UT; −14°	09:35 UT; −18°	· · ·
2011 Feb 13	17:38 UT; +17°	17:40 UT; +18°	17:44 UT; +21°
2011 Feb 15	01:56 UT; −32°	02:02 UT; −54°	02:08 UT; −63°

concentrated bright spot is removed in the data set at 08:31 UT for the automatic cross-correlation (data between 230°–265° is set to zero). The results show that the best cross-correlation of 0.46 is obtained by moving the earlier data set by −6° (slight anticlockwise rotation). The second-best correlation of 0.32 is found by moving the earlier data set by −48°. This value is consistent with the "by-eye" measurement of an ∼41° anticlockwise rotation.

4.2. 2007 December 7

There is a forward "S" sigmoid associated with the source active region NOAA AR 10977 (see the top right panel of Figure 5). Green et al. (2011) also studied this CME source region, concluding that it had positive helicity. Savcheva et al. (2012) focused on analyzing the evolution of the source region magnetic field and sigmoid development, whereas Ma et al.

(2009) studied aspects of the morphology and kinematics of this coronal wave using data from both *STEREO A* and *B*.

Here we study the expansion of the 2007 December 7 event as captured in two successive EIT 195 Å base difference images (Figure 2), at 04:34 UT and 04:46 UT. The base image used was at 04:23 UT, just prior to the start of the eruption.

Examining the mean intensity plots for the successive ellipses, two "by-eye" phase shifts of ∼+25° and +33° clockwise are suggested (top right panel of Figure 2). Taking a mean value of +29°, the resulting phase shift is shown in the middle right panel of Figure 2.

The bottom right panel of Figure 2 shows the automatically computed cross-correlation. The best cross-correlation of 0.65 is obtained by moving the earlier data set by +35°. This value is consistent with the "by-eye" measurement of an ∼25°–33° clockwise rotation.
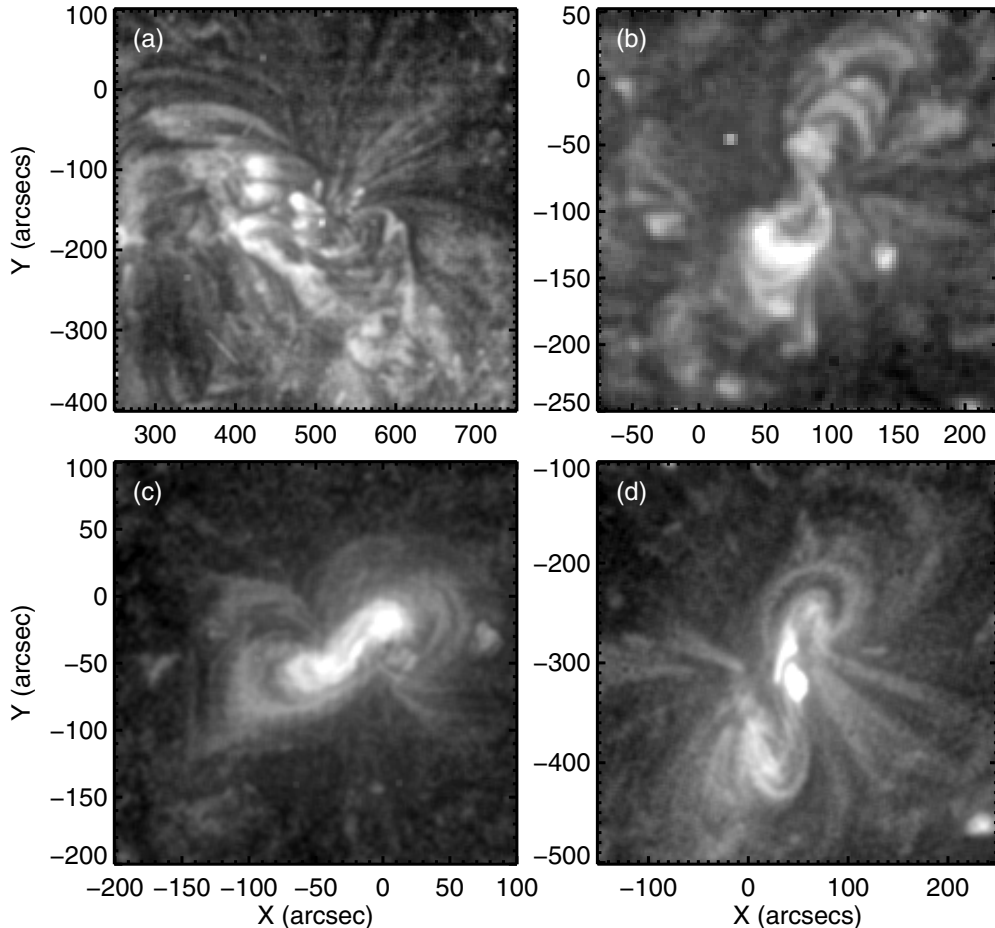
Figure 5. Source regions of events that show sigmoidal structures, prior to the eruptions. Top left shows an indication of a reverse "S" on 2006 July 6 at 07:01 UT (*SOHO*/EIT 284 Å); top right, bottom left, and bottom right panels all show forward "S"s on 2007 December 7 at 03:11 UT (*SOHO*/EIT 195 Å), 2009 February 13 at 00:06 UT (*STEREO*/EUVI(B) 284 Å), and 2010 April 3 at 06:12 UT (*Hinode*/XRT Al mesh), respectively.

4.3. 2009 February 13

This event was observed by the two *STEREO* spacecraft in almost perfect quadrature, with *STEREO-A* observing the CME on the limb, and *STEREO-B* looking at a near disk-center event. Cohen et al. (2009) studied this coronal wave using a three-dimensional, global magnetohydrodynamic model for the solar corona, focusing primarily on the lower corona, out to 3 $R_\odot$. They found that the CME becomes large scale quite low (<200 Mm) in the corona, with the expansion being facilitated by magnetic reconnection between the expanding CME core and the surrounding magnetic environment. Miklenic et al. (2011) analyzed both *STEREO* and *Hinode*/Extreme ultraviolet Imaging Spectrometer (EIS) data and focused on the temporal evolution of the dimmings. They found that the center of gravity of the dimmings rotated clockwise around the center of the flare site, and that the configuration of the dimmings exhibits the same "sheared-to-potential" evolution as the postflare loops.

Prior to the eruption, there is a forward "S" sigmoid associated with the source active region NOAA AR 1012 (indicating positive helicity). It is the only active region on the solar disk (see bottom left panel of Figure 5).

The coronal wave for the 2009 February 13 event is captured in two successive EUVI-B 195 Å base difference images (Figure 3), at 05:55 UT and 06:05 UT. The base image used was at 05:15 UT, just prior to the start of the eruption.

Examining the mean intensity plots for the successive ellipses, a "by-eye" phase shift of $\sim+12°$ (12° clockwise) is measured (top and center right panels of Figure 3).

The bottom right panel of Figure 3 shows the automatically computed cross-correlation. The best cross-correlation of 0.60 is obtained by not moving the earlier data set at all (i.e., by 0°, and thus effectively no phase shift). The second best correlation of 0.51 is found by moving the earlier data set by +15°. This value is consistent with the "by-eye" measurement of an $\sim12°$ clockwise rotation.

4.4. 2010 April 3

This event also has a forward "S" sigmoid associated with the source active region NOAA 11059 (see bottom right panel of Figure 5). Möstl et al. (2010) studied the subsequent interplanetary CME and moderate geomagnetic storm where communication with the Galaxy 15 satellite was temporarily lost. Orlando et al. (2011) studied the magnetic configuration of the CME source region, finding it to have increasing positive magnetic helicity prior to the eruption.

The coronal wave for the 2010 April 3 event is captured in two successive EIT 195 Å base difference images (Figure 4), at 09:13 UT and 09:25 UT. The base image used was at 08:47 UT, just prior to the start of the eruption.
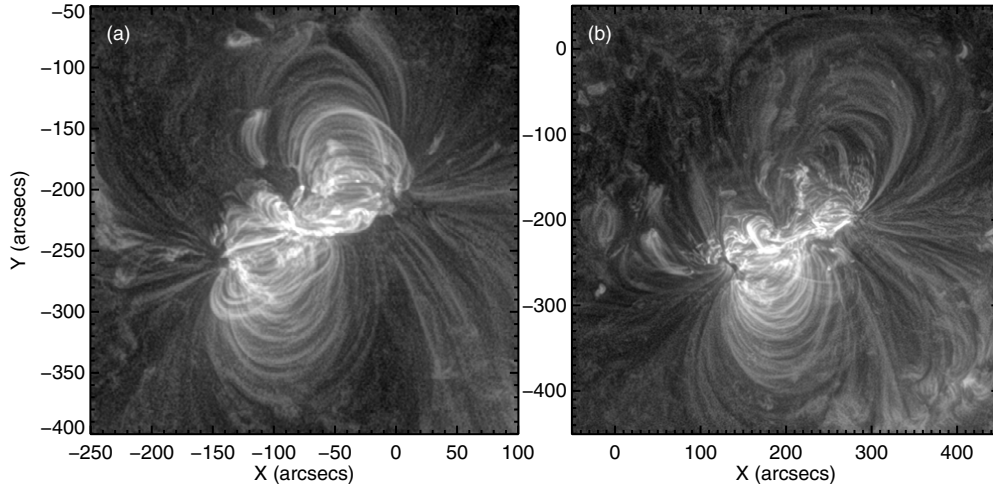
Figure 6. NOAA active region 11158, the source region of two CME events without large-scale sigmoidal structures, seen in *SDO*/AIA 211 Å data. The left panel shows an image at 17:30 UT, just prior to the eruption on 2011 February 13. The right panel shows an image at 01:40 UT, just prior to the 2011 February 15 eruption.

Examining the mean intensity plots for the successive ellipses, a "by-eye" phase shift of ∼+35° (35° clockwise) is measured (top and center right panels of Figure 4).

The bottom right panel of Figure 4 shows the automatically computed cross-correlation. The best cross-correlation of 0.44 is obtained by moving the earlier data set by +38°. This value is consistent with the "by-eye" measurement of an ∼35° rotation, clockwise.

4.5. 2011 February 13 and 15

The coronal waves of 2011 February 13 and 15 show relatively isotropic expansions. There was also an eruption on February 14, but this was asymmetric and the coronal wave expanded to the north of the source region only, making it unsuitable for this analysis.

There is no clear sigmoid associated with NOAA active region 11158, before either of the eruptions on 2011 February 13 and 15 (see Figure 6). However, the case for the presence of a flux rope in this CME source region was argued in Zharkov et al. (2011). In that paper, *Hinode*/X-Ray Telescope (XRT) data were analyzed, which hinted at a sigmoid being present at the end of the day on February 14, though the imagery was not conclusive. More significantly, the formation of the eruptive magnetic configuration and its eruption signatures (specifically the flare ribbons) were found to present evidence for the existence of a flux rope with positive helicity.

4.5.1. 2011 February 13

The coronal wave from 2011 February 13 was observed by *SDO*/AIA data with a much higher cadence than *SOHO*/EIT or *STEREO*/EUVI. The event is studied here using three *SDO*/AIA 211 Å base difference images (Figure 7), at 17:38 UT, 17:40 UT, and 17:44 UT. The base image used was at 17:33 UT, just prior to the start of the eruption.

Examining the mean intensity plots for the successive ellipses "by eye," it is not obvious that any peaks can be matched in successive data sets. There is no clear phase shift present in the data.

The right panel in Figure 7 shows the automatically computed cross-correlation between the data sets at 17:38 UT and 17:44 UT. The best cross-correlation of 0.53 is found by mov-

ing the earlier data set by −15°. This value is equivalent to a rotation of −15° anticlockwise, and is the result of aligning the largest peaks from each data set. This phase shift is applied to the mean intensity measurements and shown in the bottom two right panels of Figure 7.

4.5.2. 2011 February 15

The coronal wave for the 2011 February 15 event is studied using three *SDO*/AIA 211 Å base difference images (Figure 8), at 01:56 UT, 02:02 UT, and 02:08 UT. The base image used was at 01:30 UT, just prior to the start of the eruption.

Examining the mean intensity plots for the successive ellipses "by eye," it is again not obvious that any peaks can be matched in successive data sets, and no obvious phase shift is identifiable in the data.

The fourth right panel Figure 8 shows the automatically computed cross-correlation between the data sets at 01:56 UT and 02:08 UT. The best cross-correlation of 0.45 is obtained by moving the earlier data set by −173°. This value suggests a rotation of 173° anticlockwise, and essentially aligns the largest peaks from each data set. The second and third best correlations of 0.25 occur at +2° and +125°, respectively. Given that the high cadence of *SDO*/AIA base difference data shows no obvious substantial rotation, the most realistic phase shift of +2°, clockwise is applied to the mean intensity measurements, and shown in the two bottom right panels of Figure 8.

5. DISCUSSION

5.1. The Association of Sigmoids with Rotating Coronal Waves

We analyzed the behavior of six global EUV coronal waves linked to the eruption of pre-existing flux ropes. The results show that where a sigmoidal structure is clearly present in the CME source region, >20° rotation of the coronal wave can be expected, and measured in EUV data. Importantly, the sense of rotation of the global coronal wave during its expansion (clockwise or anticlockwise) is found to be consistent with the magnetic helicity of the CME source region (indicated by the sense of the sigmoid, being forward "S" for positive helicity with clockwise rotation, and vice versa).

The nonrotation eruptions of 2011 February 13 and 15 have been presented here as examples of nonsigmoidal CME source
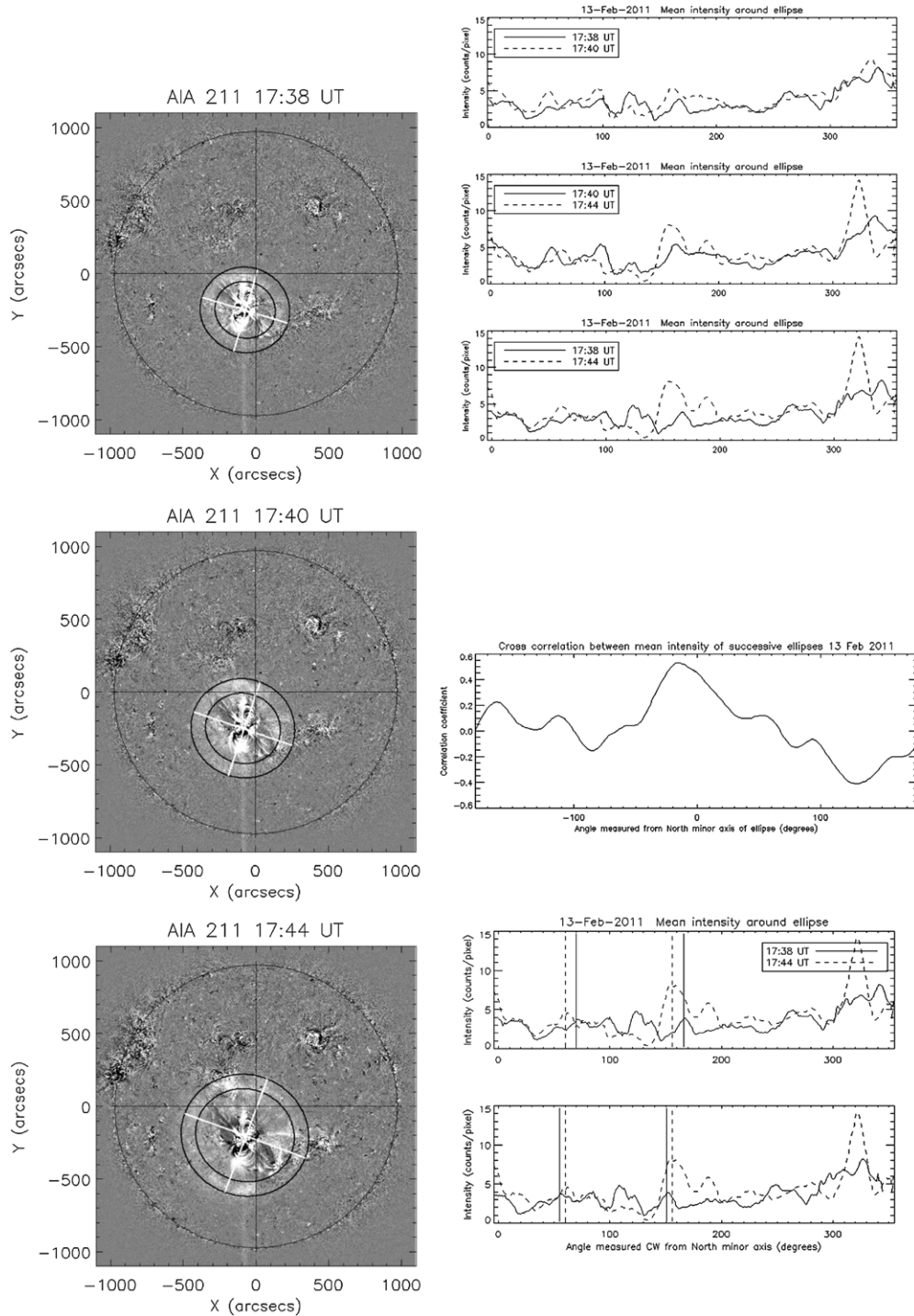
Figure 7. Left panels show the 2011 February 13 coronal wave expansion. The top right three panels show the mean intensity traces measured around the ellipses. The fourth-right panel shows the cross-correlation between the two mean intensity traces at 17:38 and 17:44 UT. The bottom right panels compare the mean intensity traces at these times and a phase-shift of $-15°$.

regions. They are nonsigmoidal in the sense that they do not possess relatively large, diffuse sigmoids, of the type visible in the hotter wavebands as observed in, e.g., *Yohkoh*/Soft X-ray Telescope (SXT) data (e.g., Canfield et al. 1999). Green et al. (2007) discuss various models for sigmoid formation, with an emphasis on the relationship between transient coronal sigmoids and erupting flux ropes. An unpublished study by C. Tincelin et al. (2014, private communication), examined one of the nonrotation events presented here, the CME eruption of

2011 February 15 that started just after 17:30 UT. They identify a relatively small, well defined "S"-shape *within* the core of the active region, from 04:50 UT, which is dominated by strong magnetic field convergence and cancellation. Measuring the angle between the neutral line and magnetic field lines, they concluded that AR 11158 possed a positive helicity. Zharkov et al. (2011) studied the 2011 February 15 event (same source AR 11158), and concluded that a model of flux rope eruption best fits the multi-spectral and magnetic field observations.
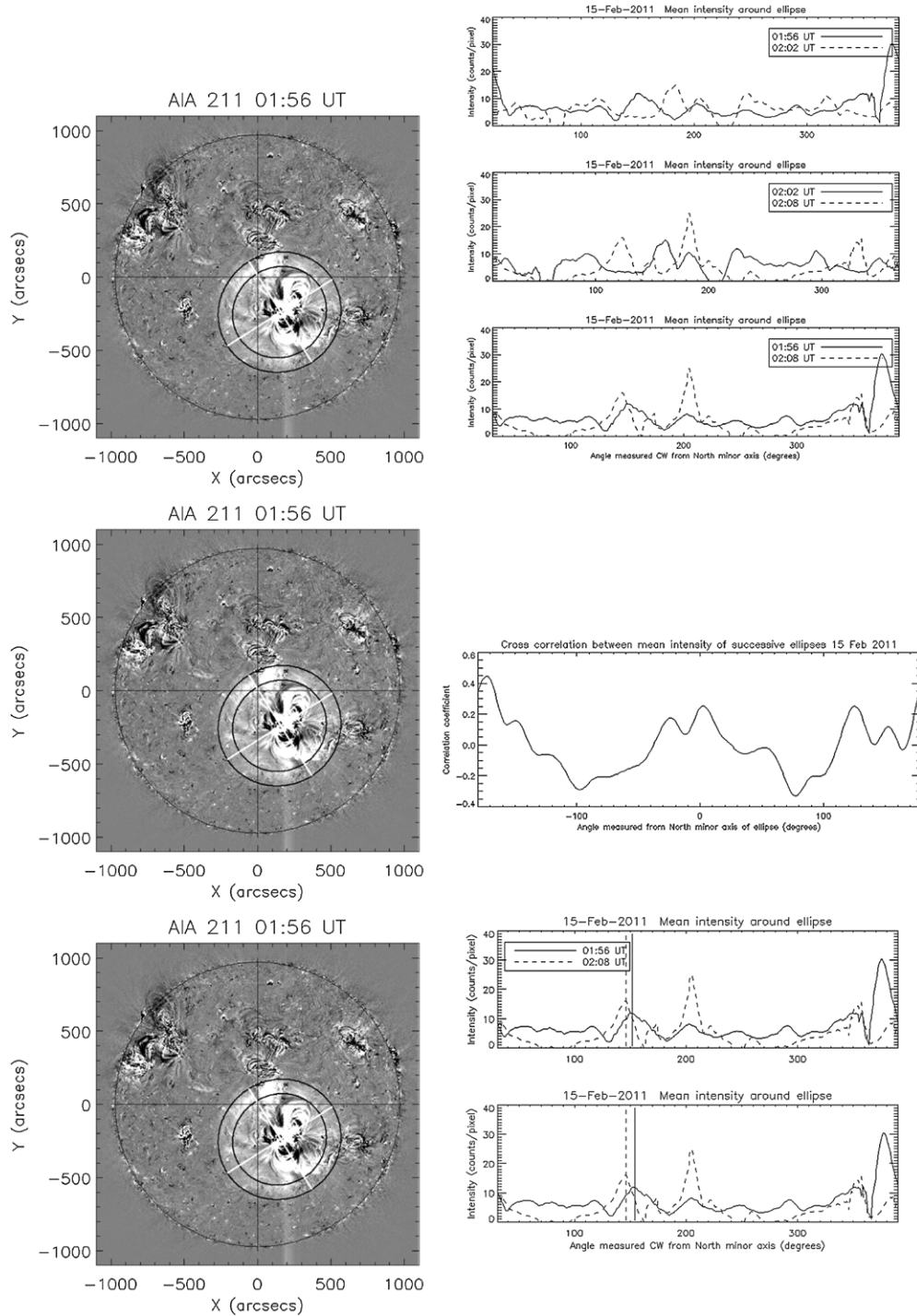
Figure 8. Left panels show the 2011 February 15 coronal wave expansion. The top right three panels show the mean intensity traces measured around the ellipses. The fourth-right panel shows the cross-correlation between the two mean intensity traces at 01:56 and 02:08 UT. The bottom right panels compare the mean intensity traces at these times and the most realistic phase-shift of +2°.

The question that begs to be asked is: "Why do only coronal waves from *Yohkoh*-type sigmoidal source regions show substantial (>20°) rotation?"

5.2. Influence of the Magnetic Field on Coronal Wave Rotation

Observations of rotating flux rope eruptions can be interpreted in the context of various instabilites. These include the torus instability (e.g., Kliem & Török 2006b; Isenberg & Forbes 2007) where a toroidal flux rope is held in equilibrium by an overlying magnetic arcade, becoming unstable when the flux rope length exceeds a critical value. The presence of an external shear magnetic field component (when crossed with the flux rope loop current) exerts a sideways Lorentz (torque) force that acts on the loop legs, forcing the rising top part of the loop to rotate. Rotations of tens of degrees can be achieved by the torus instability, which is consistent with the amounts of rotation found in the events studied here. Alternatively, twist may be relaxed, becoming converted to writhe during the CME expansion via the helical kink instability (see, e.g., Kliem et al. 2004; Török & Kliem 2005; Kliem & Török 2006a).

Kliem et al. (2012) concluded that the shear field is the dominant driver of rotations in the corona, (indeed it is required if the rotation reaches angles of the order of 90° and higher), and that it dominates even if the twist exceeds the threshold of the helical kink instability. Lynch et al. (2009) study the rotation of CMEs during eruption using numerical simulations employing initiation via the magnetic breakout model, attributing the physical origin for the observed rotation to the evolution of the Lorentz force during the initial expansion of the sheared core field. Other causes of flux rope rotation include a Lorentz force from the twisted flux rope itself, magnetic reconnection with the ambient field (Kliem et al. 2012 and references therein), and the propagation through the overlying field (including, e.g., deflection or reconnection with neighboring magnetic structures such as coronal holes). For a specific event on 2008 April 9, Kliem et al. (2012) found that reconnection of the flux rope legs with the ambient field contributes only a minor part of the total rotation in their simulation. The reconnection-driven rotation appears to remain weaker than (or at most comparable to) the twist-driven rotation, with the shear-driven rotation remaining the dominant factor.

On examining the magnetograms for the six events studied here, the *Yohkoh*/SXT-type sigmoid source regions (associated with the rotating coronal waves) have a relatively simple bipolar magnetic configuration (Figure 9, panels (a)–(d)). The two coronal wave rotation events studied by Attrill et al. (2007) also have a bipolar magnetic field structure (Figure 9, panels (e) and (f)). In contrast, the magnetograms for the source regions of the 2011 February 13 and 15 nonrotation events are made up of more complex, quadrupolar, magnetic configurations (Figure 9, panels (g) and (h)).

In both, the rotation and nonrotation cases, it is indicated that magnetic helicity is present, and the same types of forces are acting on the flux ropes. In principle, then, the possibility for rotation upon expansion is present for all cases. However, in the nonrotation cases with the more complex magnetic field source regions, it appears that the magnetic pressure of the flux rope is secondary to the pressure exerted by the surrounding magnetic field. This greater surrounding magnetic pressure acts to maintain the orientation of the flux rope axis, and the evolution of the CME when it does expand is dominated by the forces imposed by the surrounding magnetic field, rather than by the forces of the flux rope. The interaction of the active region magnetic field with the strong and complex surrounding fields may, therefore, act to mitigate the evolution of the CME flux rope expansion, preventing any discernable rotation in the coronal wave footprint. Indeed, for nonrotation events that show evidence of a pre-eruption flux rope, Kliem et al. (2012) note that other processes may counteract the rotation driven by the shear field and twist relaxation, citing magnetic reconnection with the ambient field as a plausible example.

On considering rotation, an interpretation highlighting interaction (though not reconnection) between the active region magnetic field with that of the surrounding fields is indicated by the magnetic field topology proposed by Miklenic et al. (2011) in their study of the 2009 February 13 (bipolar, rotation) event. Before the eruption begins, Miklenic et al. (2011) consider that a magnetic separatrix layer divides the flux rope from the overlying arcade that spans the polarity inversion line (PIL). The inner loops of this arcade (which are rooted closest to the PIL), are strongly sheared and low-lying. For a bipolar active region, the loop tops of the surrounding magnetic fields become successively less sheared, with the outer loops reaching to

higher and higher altitudes. On eruption, the flux rope field lines are stretched and the first dimmings appear near its footpoints (Sterling & Hudson 1997; Webb et al. 2000), at the most strongly sheared locations. When the erupting flux rope encounters the field lines of the overlying arcade, it stretches them while it continues to rise and dimmings appear near their footpoints. The dimmings associated with the stretching of each successive overlying arcade field line, therefore, appear at different times and positions, giving the impression of rotating twin dimming regions as they move away from the source region of the eruption (Miklenic et al. 2011).

The properties of global coronal waves (also known as coronal bright fronts) have been studied in multiple passbands using different instruments (e.g., Long et al. 2008, 2011; Attrill et al. 2009). It is well-recognized in the literature that coronal wave bright fronts can be due to both temperature and density enhancements (e.g., Wills-Davey & Thompson 1999; Delannée 2000; Warmuth et al. 2005; Wills-Davey 2006; Delannée et al. 2007; Schrijver et al. 2011; Downs et al. 2012). Taking the view that diffuse coronal wave bright fronts are (at least in some part) due to plasma compression, we can augment the picture of evolving magnetic field topology proposed by Miklenic et al. (2011, their Figure 10) to include the rotating coronal wave bright fronts as studied in this paper. Early in the expansion, the bright front peaks identified in the first images shown in Figures 1–4 lie at a larger radius than the dimmings, but are located along approximately the same imaginary guide line (drawn from the center of the eruption site to the outer ellipse). By the time of the second image, the dimmings lie in approximately the same location (albeit some rotation may be indicated, similar to that observed by Miklenic et al. 2011). However, at the larger radius, the peak of the bright front has rotated off of the guide line for the earlier bright peak (see Figure 3, Attrill et al. 2007). This is consistent with the picture of an expanding flux rope stretching (and compressing plasma) at the interface with successively larger and increasingly potential magnetic field lines, while the flux rope footpoints remain relatively fixed. In this picture, one may conclude that rotation of the flux rope could occur independent of either the kink or torus instabilities, with eruptions from bipolar regions being expected to undergo a rotation of the expanding flux rope simply facilitated by the expansion against progressively less sheared overlying magnetic field. However, Kliem et al. (2012) find that in the low-beta corona, the changing orientation of the vertical field component's polarity inversion line with height is not the primary driver for flux rope rotation, (though the ambient field's height profile is found to influence the amount of rotation, particularly in occurrences of the kink instability).

The precise location of the coronal wave peak intensity can be expected to occur where the flux rope interfaces with the magnetic topology of the surrounding environment and the plasma is compressed to the greatest extent. This concentrates the peak intensity at successively displaced locations, giving rise to a rotating coronal wave as it expands away from the source region of the eruption. Evidence for this can be found in some coronal wave rotation events, where there are two peaks in intensity, separated by approximately 180°. These events include: 1997 April 7 and 1997 May 12 (Attrill et al. 2007) and 2007 December 7 and 2010 April 3 (this paper).

Close to the PIL, the overlying arcade consists of low-lying, strongly sheared loops. This remains the case whether the surrounding magnetic field is simple (e.g., bipolar) or complex (e.g., quadrupolar—as evidenced by the presence of
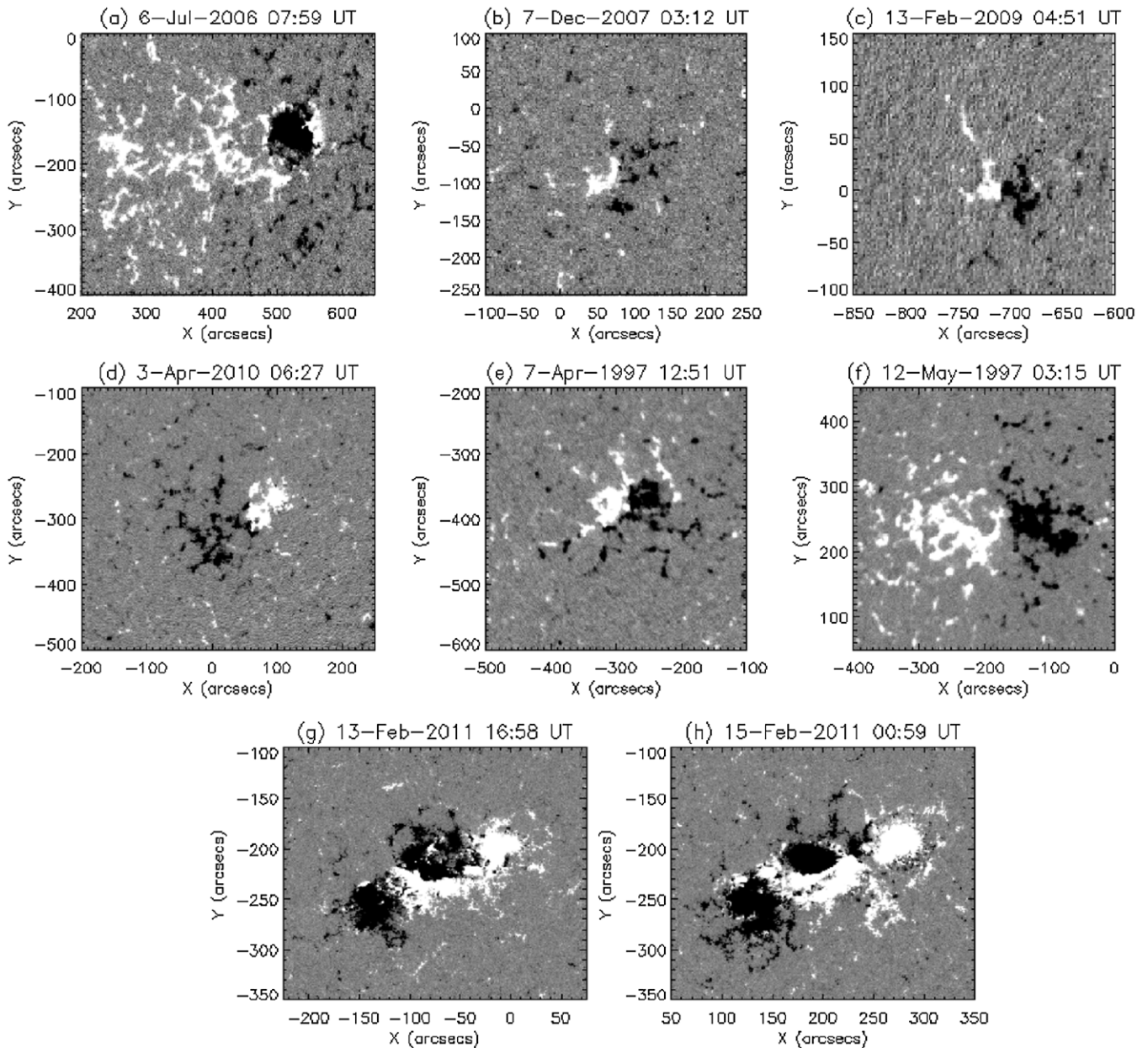
Figure 9. Magnetograms showing the source regions of the CME-coronal wave events, scaled to ±100 G. Panels (a)–(d) are from the four events in this study that show a clear rotation. Panels (e) and (f) are the source regions of the two rotation events presented in Attrill et al. (2007). The source regions of all six of these rotating events have a largely bipolar magnetic field configuration. Panels (g) and (h) show the source regions of the nonrotation events seen in 2011 February. These CMEs originate from quadrupolar regions, where the magnetic field is more complex.

the small sigmoid confined within AR 11158 in the quadrupolar 2011 February events. Where the surrounding magnetic field is complex, it may not be reasonable to assume that at greater distances from the PIL, the amount of shearing decreases with increasing loop top altitude in an orderly manner. In such instances, clear coronal wave rotation is, therefore, not observed.

5.3. Linking Observations of ICME Rotation to Source Region Properties

A study by Yurchyshyn et al. (2009) compared the orientation angles of elongated LASCO CMEs (which they previously showed corresponds well to the orientation of the underlying flux rope; Yurchyshyn 2008), to post-eruption arcades (PEAs), as observed in *SOHO*/EIT data. By analyzing a sample of 100

events, they found that the overwhelming majority of CMEs are elongated in the direction of the axial field of PEAs, with 70% of CMEs appearing to rotate by only about 10° during their evolution. However, a more substantial rotation of 30°–50° was found for some events. Although Yurchyshyn (2008) suggest that the rotation of the CME may be due to the presence of the heliospheric current sheet shaping the expansion, Kliem et al. (2012) comment that if this were the dominant effect, the rotation of erupting flux could be predicted rather straightforwardly from extrapolation of the photospheric field, since the overlying field is often close to potential. However, such a conjecture is not valid in the lower corona where $\beta \ll 1$, and where the main part of the total CME volume rotation is often found to occur. Indeed, it is known that more dynamic features low down in the solar corona may strongly impact the

CME expansion and resulting ICME structure (e.g., interaction with "open" coronal hole magnetic fields Attrill et al. 2006; Crooker & Webb 2006; Baker et al. 2007).

The processes that effect the outcome of an eruption and its final magnetic orientation are complex. For example Harra et al. (2007) studied eruptions from the same active region, on successive days in 2004 November, and found that they produced oppositely directed magnetic clouds. From analysis of interplanetary scintillation data, the second CME was found to be influenced by a dynamic tongue of high-speed plasma that may have been driven by the previous CME. Harra et al. (2007) consider that the apparent rotation of the second CME may have been caused by the large-scale dynamics and interaction between different parts of the ejection, which included a large-scale transequatorial filament and loops system. The overall development of an expanding CME is likely to be a combination of influences from both the heliospheric magnetic field and the more dynamic lower-corona forces. Being able to predict which one is likely to dominate for a given eruption could allow a useful insight into the expected CME evolution and subsequent orientation in the near-Earth environment.

6. CONCLUSIONS

In addition to the 1997 April 7 and May 12 events studied in Attrill et al. (2007), here we have presented the analysis of a further six global coronal wave events. All events show supporting evidence for the existence of pre-eruption flux ropes. In total, we find: two events with a reverse "S" sigmoid, which exhibit a >20° anticlockwise rotation; four events with a forward "S" sigmoid, three of which exhibit a >20° clockwise rotation (the remaining event also showing a clockwise rotation, but only of ∼15°) and two events with no clear sigmoid, where no phase shift is observed. On examining the magnetic configuration of the source regions, we find that these latter (nonrotation) events possess a quadrupolar magnetic configuration. The coronal waves that do show a measurable rotation originate from bipolar source regions.

The direction of the coronal wave rotation (clockwise or anticlockwise) is found to be consistent with the sense of magnetic helicity (positive or negative, respectively) of the CME source region. The results presented here are, therefore, consistent with the initial detection of coronal wave rotation in the 1997 May 12 event by Podladchikova & Berghmans (2005), and the finding that the direction of rotation is dependent on the sense of helicity of the CME source region as reported by Attrill et al. (2007).

REFERENCES

Attrill, G., Nakwacki, M. S., Harra, L. K., et al. 2006, SoPh, 238, 117
Attrill, G. D. R. 2008, PhD thesis, University College London, 239
Attrill, G. D. R. 2010, ApJ, 718, 494
Attrill, G. D. R., Engell, A. J., Wills-Davey, M. J., Grigis, P., & Testa, P. 2009, ApJ, 704, 1296
Attrill, G. D. R., Harra, L. K., van Driel-Gesztelyi, L., & Démoulin, P. 2007, ApJL, 656, L101
Attrill, G. D. R., van Driel-Gesztelyi, L., Démoulin, P., et al. 2008, SoPh, 252, 349
Baker, D., van Driel-Gesztelyi, L., & Attrill, G. D. R. 2007, AN, 328, 773
Biesecker, D. A., Myers, D. C., Thompson, B. J., Hammer, D. M., & Vourlidas, A. 2002, ApJ, 569, 1009
Canfield, R. C., Hudson, H. S., & McKenzie, D. E. 1999, GeoRL, 26, 627
Chertok, I. M., & Grechnev, V. V. 2005, SoPh, 229, 95
Cliver, E. W., Laurenza, M., Storini, M., & Thompson, B. J. 2005, ApJ, 631, 604
Cohen, O., Attrill, G. D. R., Manchester, W. B., IV, & Wills-Davey, M. J. 2009, ApJ, 705, 587
Crooker, N. U., & Webb, D. F. 2006, JGRA, 111, 8108
Deforest, C. E. 2004, SoPh, 219, 3
Delaboudinière, J.-P., Artzner, G. E., Brunaud, J., et al. 1995, SoPh, 162, 291
Delannée, C. 2000, ApJ, 545, 512
Delannée, C., Hochedez, J.-F., & Aulanier, G. 2007, A&A, 465, 603
Domingo, V., Fleck, B., & Poland, A. I. 1995, SoPh, 162, 1
Downs, C., Roussev, I. I., van der Holst, B., Lugaz, N., & Sokolov, I. V. 2012, ApJ, 750, 134
Driesman, A., Hynes, S., & Cancro, G. 2008, SSRv, 136, 17
Gallagher, P. T., & Long, D. M. 2011, SSRv, 158, 365
Green, L. M., Kliem, B., Török, T., van Driel-Gesztelyi, L., & Attrill, G. D. R. 2007, SoPh, 246, 365
Green, L. M., Kliem, B., & Wallace, A. J. 2011, A&A, 526, A2
Harra, L. K., Crooker, N. U., Mandrini, C. H., et al. 2007, SoPh, 244, 95
Isenberg, P. A., & Forbes, T. G. 2007, ApJ, 670, 1453
Jiang, Y., Yang, L., Li, K., & Ren, D. 2007, ApJL, 662, L131
Kaiser, M. L., Kucera, T. A., Davila, J. M., et al. 2008, SSRv, 136, 5
Kliem, B., Titov, V. S., & Török, T. 2004, A&A, 413, L23
Kliem, B., & Török, T. 2006a, BAAS, 38, 234
Kliem, B., & Török, T. 2006b, PhRvL, 96, 255002
Kliem, B., Török, T., & Thompson, W. T. 2012, SoPh, 281, 137
Leamon, R. J., Canfield, R. C., & Pevtsov, A. A. 2002, JGRA, 107, 1234
Lemen, J. R., Title, A. M., Akin, D. J., et al. 2012, SoPh, 275, 17
Liu, W., & Ofman, L. 2014, SoPh, 289, 3233
Long, D. M., DeLuca, E. E., & Gallagher, P. T. 2011, ApJL, 741, L21
Long, D. M., Gallagher, P. T., McAteer, R. T. J., & Bloomfield, D. S. 2008, ApJL, 680, L81
Lynch, B. J., Antiochos, S. K., Li, Y., Luhmann, J. G., & DeVore, C. R. 2009, ApJ, 697, 1918
Ma, S., Wills-Davey, M. J., Lin, J., et al. 2009, ApJ, 707, 503
McIntosh, S. W., Leamon, R. J., Davey, A. R., & Wills-Davey, M. J. 2007, ApJ, 660, 1653
Miklenic, C., Veronig, A. M., Temmer, M., Möstl, C., & Biernat, H. K. 2011, SoPh, 273, 125
Moreton, G. E. 1960, AJ, 65, 494
Moreton, G. E., & Ramsey, H. E. 1960, PASP, 72, 357
Moses, D., Clette, F., Delaboudinière, J.-P., et al. 1997, SoPh, 175, 571
Möstl, C., Temmer, M., Rollett, T., et al. 2010, GeoRL, 37, 24103
Orlando, A., Zuccarello, F., Romano, P., et al. 2011, in IAU Symp. 274, Advances in Plasma Astrophysics, ed. A. Bonanno, E. de Gouveia Dal Pino, & A. G. Kosovichev (Cambridge: Cambridge Univ. Press), 165
Patsourakos, S., & Vourlidas, A. 2012, SoPh, 281, 187
Patsourakos, S., Vourlidas, A., & Kliem, B. 2010, A&A, 522, A100
Pesnell, W. D., Thompson, B. J., & Chamberlin, P. C. 2012, SoPh, 275, 3
Pevtsov, A. A., Canfield, R. C., & McClymont, A. N. 1997, ApJ, 481, 973
Podladchikova, O., & Berghmans, D. 2005, SoPh, 228, 265

Rust, D. M. 1983, SSRv, 34, 21
Rust, D. M., & Kumar, A. 1996, ApJL, 464, L199
Savcheva, A. S., Green, L. M., van Ballegooijen, A. A., & DeLuca, E. E. 2012, ApJ, 759, 105
Schrijver, C. J., Aulanier, G., Title, A. M., Pariat, E., & Delannée, C. 2011, ApJ, 738, 167
Sterling, A. C., & Hudson, H. S. 1997, ApJL, 491, L55
Thompson, B. J., Plunkett, S. P., Gurman, J. B., et al. 1998, GeoRL, 25, 2465
Török, T., & Kliem, B. 2005, ApJL, 630, L97
Török, T., Temmer, M., Valori, G., et al. 2013, SoPh, 286, 453
Uchida, Y. 1968, SoPh, 4, 30

Warmuth, A., Mann, G., & Aurass, H. 2005, ApJL, 626, L121
Webb, D. F., Lepping, R. P., Burlaga, L. F., et al. 2000, JGR, 105, 27251
Wills-Davey, M. J. 2006, ApJ, 645, 757
Wills-Davey, M. J., & Attrill, G. D. R. 2009, SSRv, 149, 325
Wills-Davey, M. J., & Thompson, B. J. 1999, SoPh, 190, 467
Wülser, J.-P., Lemen, J. R., Tarbell, T. D., et al. 2004, Proc. SPIE, 5171, 111
Yurchyshyn, V. 2008, ApJL, 675, L49
Yurchyshyn, V., Abramenko, V., & Tripathi, D. 2009, ApJ, 705, 426
Zharkov, S., Green, L. M., Matthews, S. A., & Zharkova, V. V. 2011, ApJL, 741, L35
Zhukov, A. N. 2011, JASTP, 73, 1096